Spatial considerations on electrical resistance tomography measurements

2014 Meas. Sci. Technol. 25 055303

(http://iopscience.iop.org/0957-0233/25/5/055303)

IOP Publishing Measurement Science and Technology
Meas. Sci. Technol. 25 (2014) 055303 (12pp) doi:10.1088/0957-0233/25/5/055303

Spatial considerations on electrical resistance tomography measurements

John S Lioumbas, Ariadni Chatzidafni and Thodoris D Karapantsios

Division of Chemical Technology, Department of Chemistry, Aristotle University of Thessaloniki, University Box 116, 541 24 Thessaloniki, Greece

E-mail: karapant@chem.auth.gr

Received 5 November 2013, revised 27 December 2013
Accepted for publication 9 January 2014
Published 19 March 2014

Abstract

This work reports experimental evidence of the effect of certain geometrical parameters on the accuracy of electrical resistance tomography (ERT) measurements in two-phase systems. Emphasis is given to millimetre-size electrodes that suffer from significant electric field distortion due to (a) extension of the measuring volume beyond the electrode plane (fringe effect) and (b) the non-uniform distribution of field strength at the electrode plane. Water constitutes the continuous (conductive) phase, whereas Teflon rods constitute the dispersed (non-conductive) phase. The examined parameters include the diameter of the cylindrical test vessel, the size of electrodes and the number and size (radius and length) of the submerged Teflon rods. The variable in these tests is the axial and radial position of the Teflon rods inside the test cell. It is found that for homogeneously (axially and radially) dispersed rods, the void fraction measured by a set of electrodes at a plane agrees pretty well with 2D theoretical predictions. However, in cases of non-homogeneously dispersed rods, void fraction measurements deviate considerably from theoretical values. This is a manifestation of severe electric field distortion associated with the employed small electrodes. Moreover, evidence is provided that in the examined system, the fringe effect is more significant than the topography of the field strength in distorting measurements. To allow a quantitative analysis of the present data, nonlinear regression combined with dimensional analysis is conducted to derive an expression that describes the void fraction measurements by a set of electrodes at a plane for different axial and radial positions of the submerged rods. A parametric analysis of this expression illustrates the significance of different parameters on ERT measurements.

Keywords: electrical resistance technique, validation, void fraction, fringe effect

(Some figures may appear in colour only in the online journal)

1. Introduction

Electrical tomographic techniques (ETTs, i.e. electrical impedance tomography, electrical capacitance tomography and electrical resistance tomography, ERT) are used for visualizing the spatial distribution of electrical properties inside a continuous conductive volume within which non-conductive objects are dispersed. This is done by injecting sequences of low-frequency currents across a *planar slice* of the volume (electrode plane) and acquiring sets of voltage measurements from all combinations of electrode pairs (Polydorides 2002). ETTs, characterized also as soft-field techniques (electric field distribution depends on phase distribution), are recognized as low-cost, safe, portable and non-intrusive techniques with rapid response. In applications where a non-conductive gas/liquid/solid phase is dispersed inside a conductive liquid phase (e.g. bubbly flow, gas–water–oil flow in pipes, sloshing, etc), ERTs remain popular as a qualitative imaging tool in, e.g., industrial applications (Sharifi and Young 2013), geophysical applications (Dobecki and Upchurch 2006), non-destructive testing and medical diagnostic tools (Pikkemaat *et al* 2012). ERT follows the basic principles of any soft-field technique but it reconstructs only the resistivity distribution due to the

absence of phase readings in the data. The main drawback of every soft-field imaging technique is the relatively *poor spatial resolution* of the reconstructed images due to the distortion of the electric field (Chin 2011). The reasons for this are: (a) the so-called *fringe* or three-dimensional (3D) *effect* and (b) the *topography of the field strength*.

(a) The *fringe effect* is the result of 3D extension of the electrical field (Li and Yang 2009). Specifically, the fringe effect refers to a sensing region which is not constrained within the electrode plane (cross-section of the test vessel), but extends to an appreciable volume above and below it. This effect is worse for small-size (pin) electrodes. Recent experimental and theoretical studies have shown that the fringe effect can be suppressed by increasing the measuring volume, e.g., by increasing the length of electrodes (Sun and Yang 2012, 2013). Unfortunately, this practice leads to a wide measuring volume which sacrifices the local character of measurements but can still be useful for monitoring average features of spatially homogeneous flows, e.g. stationary/ergodic (mean value and auto-correlation function of void fraction are steady among sampling periods) bubbly and stratified flows. Needless to say, this practice cannot be applied to spatially non-homogeneous applications (e.g. non-stationary/ergodic dispersed flows, sloshing), where the measuring volume needs to be as narrow as possible to be able to give meaningful information. Furthermore, Sun and Yang (2013) employed end-guards as another means to diminish the fringe effect. Although that effort has been quite successful for the examined test pipes, it remains to be explored over a broad range of geometrical conditions, e.g. smaller diameter pipes and smaller electrodes, before conclusive statements can be made. In any case, in order to take suitable countermeasures, one should have an idea of the extent of the fringe effect. And this is indeed at the core of this work. To the best of our knowledge, there are no studies that quantitatively investigate how the fringe effect is influenced by the distance between dispersed non-conductive objects and the measuring plane or/and by the objects' size (radius and length). This is critical for millimetre-size electrodes where the fringe effect is substantial.

(b) The *topography of the field strength* at any point inside the measuring volume is a function of the distribution of electrical properties throughout this volume (i.e. ill-posedness problem of image reconstruction). The above phenomenon is caused by the low-frequency and long wavelength electromagnetic radiation that is employed by any soft-field technique (Polydorides 2002). In other words, the field sensitivity (Wang *et al* 2012) is influenced by both (i) the size and the physical properties of the components and (ii) the distribution of the objects inside the measuring volume. For small-size electrodes, there is a high density of electric lines (high field strength) close to the electrodes, which however dilute gradually towards the centre of the measuring volume. So objects near the electrodes have a stronger effect on measurements than those at the centre of the measuring volume (Sun and Yang 2013).

Every known study that aims at the experimental validation of ERT (Kim *et al* 2011, 2012, 2013, Fan and Wang 2010) focuses on the capability of a 2D algorithm to predict the shape and the position of one or more stationary objects. Nevertheless, most real tests are performed employing *infinite*-length objects (large length compared to the sensors' size and the width of the measuring volume) located at different radial positions inside the measurement volume. This approach is good for capturing the fringe effect with respect to the radial position but is not capable of quantifying the effect of the axial position. To the best of our knowledge, there is no systematic study where the dimensions of dispersed objects (e.g. diameter and length) and their 3D relative positions inside the measuring volume are *theoretically* or *experimentally* considered as a parameter that could affect measurements. Recently, Sharifi and Young (2013) pointed out that in many processes that can be both temporally and spatially non-homogeneous (i.e. bubbly flow), the size and distribution of the dispersed phase will have a severe effect on image reconstruction. Furthermore, they noted the absence of studies that investigate the capability of the soft-field techniques in recognizing different sizes or/and the distribution of dispersed phase in a continuous medium.

The objective of this study is twofold.

First, to experimentally investigate how the fringe effect and the topography of the ERT field strength influence void fraction measurements of well-defined multi-dispersed systems. This is achieved by varying the radial and axial position of non-conducting Teflon rods of different radii and lengths inside a cylindrical test vessel filled with water. The dimensions of the electrodes (in millimetre range) and the diameter of the test cell (in centimetre range) are also varied. The values of the void fraction measured from a set of electrodes at a plane are employed as a means to quantify the accuracy of ERT imaging.

Second, to develop an empirical model capable of describing the experimental void fraction from a set of electrodes at a plane for any given set of system parameters and then use it to quantify the significance of these parameters in the measurements. The merit of this model extends beyond the current application to any soft-field technique.

2. Materials and methods

Instead of using our custom-made ERT, which we have customarily applied to different multiphase systems (Karapantsios and Papara 2008, Kostoglou *et al* 2010), a commercial ERT system (P2000, ITS Ltd) is employed herein that has been tested before in a wide diversity of applications (Alaqqad *et al* 2012, Stanley *et al* 2002). This will allow others to make comparisons and apply the present findings directly to their case. The ERT system consists of the data acquisition unit with the excitation current source, the sensor with its electrodes and a computer furnished with the supervising software and the reconstruction code (figure 1(*a*)). The ERT system applies a constant alternating current to a pair of electrodes and measures the voltage differences between the other electrode pairs on a plane using an adjacent-electrode

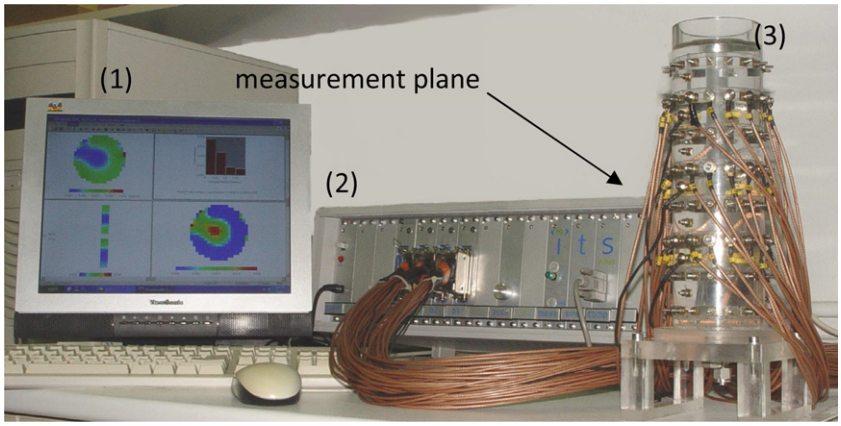

Figure 1. Experimental setup: (1) supervising computer with reconstruction code; (2) data acquisition unit with current source; (3) test vessel with tomography sensors (planes) at eight heights (only the sensor at mid-height is used here).

Table 1. Test protocol with dimensions and placement of the rods used.

		D= 2.1 cm		D= 7.0 cm		
		d, cm	**0.1, 0.3, 0.7**	**0.6, 0.7, 2,5, 4.9**	**1.0**	**2.3**
One rod	**Axial** displacement (rods are placed at: 2r/D =0) (step=0.2cm)	l, cm	0.7	30.0	0.7	0.7
					2.0	2.0
					3.0	3.0
					4.0	4.0
					6.0	6.0
					30.0	30.0
	Radial displacement (rods are placed at: 2z/d =0, ±0.5) (step 0.5cm)	l, cm	0.7		0.7	0.7
					3.0	3.0
					6.0	6.0
Two rods				1st rod, (d, ℓ) =(1, 3cm)	2nd rod, (d, ℓ) =(1, 3cm)	
				1st rod is placed at: • 2z/D = 0, 0.3, 0.5 • 2r/D = 0	2nd rod is placed at: • 2z/D = 0, ±0.5 • 2r/D ≠ 0 (radial step =0.5 cm)	
More than two rods				Various rods are placed at 4 different positions		

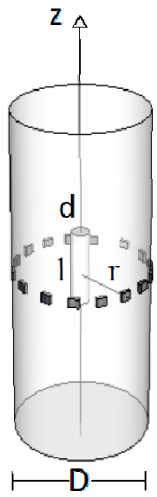

pair measurement strategy (Fransolet *et al* 2002). Preliminary tests concerning the minimization of measurement errors at a reasonable computer load lead to the following values of the sampling parameters: sampling time interval = 100, samples per frame = 8, delay cycles = 20, which yield a sampling frequency, f, of 1.6 Hz. The value of the injection current is 8 mA. The *sensitivity conjugate gradients* algorithm is employed to solve the inverse ill-posed problem of image reconstruction from resistivity measurements. The algorithm is solved in dense mesh geometry (1600 elements) after 10 steps of image reconstruction, 841 forward iterations and 3 inverse iterations. The reconstruction time is 3.04 min and the level of the measurement noise ∼0.1%.

Two cylindrical test vessels are employed with height and diameter (H, D) = (11 cm, 2.1 cm) and (26 cm, 7 cm), respectively. Only one sensor plane is used at mid-height of each test vessel. Each sensor plane consists of 16 stainless steel electrodes flush mounted on the inside wall of these vessels, spaced apart by equal intervals (22.5°) around the vessels' periphery. Electrode height and width are (l_{el}, d_{el}) = (0.5 cm, 0.2 cm) and (0.7 cm and 0.7 cm) for the small and large cylindrical test vessels, respectively. The continuous

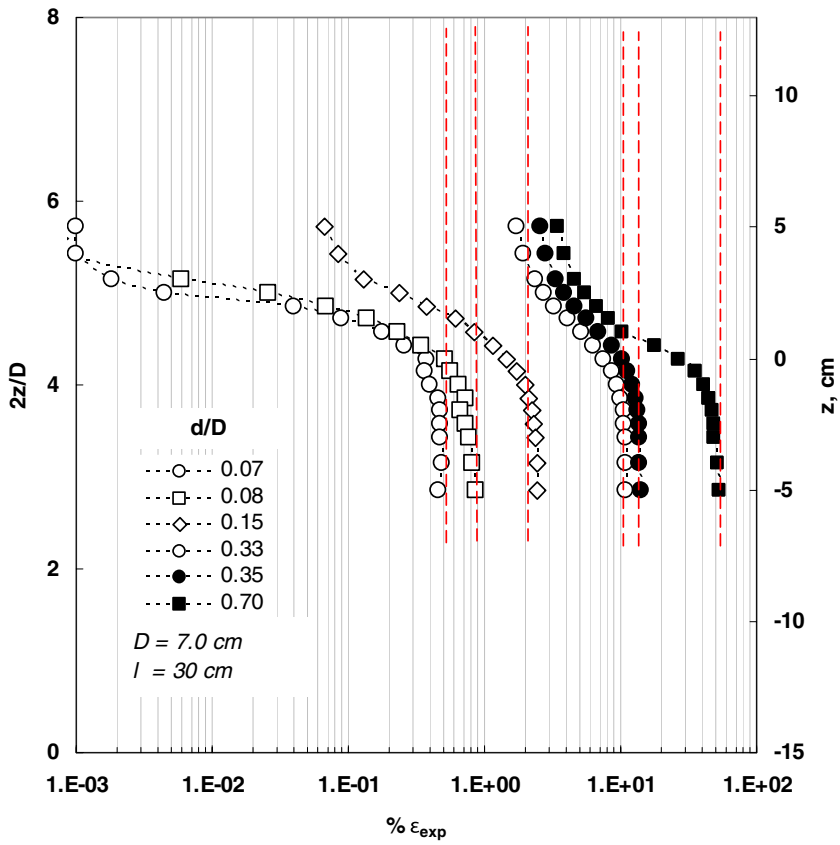

Figure 2. Effect of rod *diameters* on the measured void fractions for different axial placements of very long rods ($l = 30$ cm) in the large test vessel ($D = 7.0$ cm). In the axial direction, the geometrical centre of electrodes is at $z = 0$. In the radial direction, the vertical symmetry axis of rods coincides with the vertical symmetry axis of the vessel ($r = 0$). The red dashed lines stand for theoretical void fractions. Placement of rods is defined as: (left axis) the distance of their geometrical centre from the centre of the measurement plane normalized with respect to $D/2$; (right axis) the distance of their lower end from the centre of the measurement plane.

phase inside the vessels is deionized water/NaCI solution with electrical conductivity $\sigma_{\mathrm{cm}} = 45\ \mu\mathrm{S\ cm}^{-1}$ (measured at 25 °C, DR Lange ECM, MULTI pH-O_2-Ms, Berlin). The dispersed phase consists of Teflon (PTFE) rods with electrical conductivity that can be safely considered as zero ($\sigma_{\mathrm{PTFE}} = 10^{-20}\ \mu\mathrm{S\ cm}^{-1}$).

The test protocol and the dimensions (radius and length) of the dispersed Teflon rods are presented in table 1. We used 17 different rods at more than 50 different positions inside the vessels. In table 1, the placement of the rods is defined as the distance of their geometrical centre from the plane defined by the geometrical centre of electrodes. The rods are hanging from strong torsion wires (diameter 0.15 mm) used in thermogravimetric devices. These wires are connected to a 3D translation–positioning unit equipped with micro-metering mechanisms (accuracy ± 0.1 mm).

Analysis of measurements is based on the comparison between the 2D theoretical void fraction, $\varepsilon_{\mathrm{th}}$, and the experimental void fraction, $\varepsilon_{\mathrm{exp}}$. The 2D theoretical void fraction is calculated with the help of equation (2.1) since the cross-sectional area of the test vessels, A_{test}, and the cross-sectional area of every dispersed object, A_{obj}, are known:

$$\varepsilon_{\mathrm{th}} = \frac{A_{\mathrm{obj}}}{A_{\mathrm{test}}}. \tag{2.1}$$

$\varepsilon_{\mathrm{exp}}$ values are calculated with the help of the Maxwell equation (2.2), which relates conductivity to void fraction (George *et al* 2000):

$$\varepsilon = \frac{2\sigma_1 + \sigma_2 - 2\sigma_{\mathrm{mc}} - \frac{\sigma_{\mathrm{mc}}\sigma_2}{\sigma_1}}{\sigma_{\mathrm{mc}} + 2(\sigma_1 - \sigma_2) - \frac{\sigma_{\mathrm{mc}}\sigma_2}{\sigma_1}} \tag{2.2}$$

where σ_1, σ_2 and σ_{mc} are the conductivities of the continuous phase, the dispersed phase and the measured one, respectively. In the present case, $\sigma_2 \approx 0$ and equation (2.2) transforms to

$$\varepsilon_{\mathrm{exp}} = \frac{2\sigma_1 - 2\sigma_{\mathrm{mc}}}{2\sigma_1 + \sigma_{\mathrm{mc}}}. \tag{2.3}$$

3. Results

3.1. Rods of large length

The aim of these tests is the examination of the ERT response when objects with apparently 'infinite' length are placed inside the measuring volume. For this reason, we used Teflon rods with large length, $l = 30$ cm (which can approximately be considered as infinite compared to the electrodes length), in a wide range of diameters. To some extent, these 'infinite'-length rods simulate the behaviour of actual multiphase systems with axially homogeneous distributions of large voids (e.g. stationary/ergodic bubbly and stratified flows).

3.1.1. One rod. Figure 2 presents experimental void fraction, ε_{exp}, profiles for very long rods of different diameters positioned vertically at various locations along the axial direction. The left axis of figure 2 ($2z/D$) presents the distance between the geometrical centre of the rods and the centre of the measurement plane ($z = 0$) normalized with respect to the radius ($D/2$) of the test vessel. The right axis (z) presents the distance between the lower end of the rods and the centre of the measurement plane ($z = 0$). For the examined rods, z spans from 5 to -5 cm and $2z/D$ from 5.7 to 2.85. The vertical symmetry axis of the rods coincides with the vertical symmetry axis of the vessel ($r = 0$), i.e., rods are placed at the centre of the cross-section of the test vessel. The dashed red lines represent the theoretical void fraction values, ε_{th}, calculated from equation (2.1).

It is seen that ERT can sense the bottom of rods even far (5 cm) above the electrode plane. This implies fictitious values of the void fraction at the electrode plane. These fictitious ε_{exp} attain higher values at larger rod diameters, and although they are much lower than theoretical values, ε_{th}, they are not negligible. Only for the smaller diameter rods (i.e. $d/D < 0.08$) do the ε_{exp} values tend to zero for distances larger than $2z/D \gtrsim 5$. For rods of larger diameter (i.e. $d/D > 0.08$), the ε_{exp} values are appreciable in all examined locations of the rods. For distances $2z/D \lesssim 4$, the rods' bottoms lie below the electrode plane and the ε_{exp} values converge to ε_{th} values ($\text{dev}_{exp} < \pm\ 10\%$) regardless of the rod diameter; dev_{exp} stands for the percentage deviation of the measured values from the theoretical ones and is estimated using equation (3.1):

$$\text{dev}_{exp} = 100 \times \frac{\varepsilon_{exp} - \varepsilon_{th}}{\varepsilon_{th}}. \tag{3.1}$$

In other words, if $\pm 10\%$ deviation is taken as an acceptable approximation of ε_{th}, then ERT measures the correct void fraction as long as the rod intersects the electrode plane. For $2z/D \lesssim 3$, the ε_{exp} and ε_{th} values practically coincide. This corresponds to homogeneously (axially and radially) dispersed rods.

3.1.2. Multiple rods. In order to examine the ERT response in the presence of more than one rod, we have placed several long rods non-symmetrically inside the test vessel. The rods are again placed vertically with respect to the electrode plane but now their bottoms touch the bottom of the vessel. The tomograph insets in figure 3 indicate that ERT identifies the rods' positions fairly well (their actual positions are marked with thin circles). The theoretical estimations of the expected void fractions are marked with red dashed lines. Figure 3 demonstrates that for very long rods ($l = 30$ cm) with small diameters (i.e. $d/D = 0.08$ and 0.10), the ε_{exp} values are always higher than the corresponding ε_{th}. Specifically, dev_{exp} is calculated to 20% for any examined rod's position. The blue dashed lines stand for the void fraction values calculated by multiplying the number of rods with the ε_{exp} values of a single rod. Figure 3 shows that in most cases the ε_{exp} values coincide with the dashed blue line. The latter implies that when several rods of different diameters are placed inside the test volume, the total experimental void faction value, E_{exp}, is described by equation (3.2):

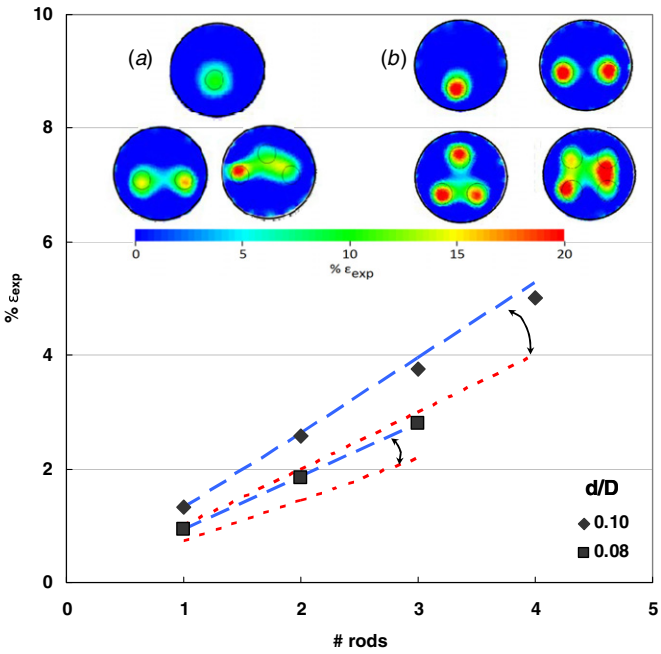

Figure 3. Tomographs for different numbers and sizes of rods placed vertically but non-symmetrically inside the test vessel. Data points are experimental void fraction values obtained by a set of electrodes at mid-height of the test vessel. The blue dashed lines stand for the void fraction values calculated by multiplying the number of rods with the experimental void fraction of a single rod: (*a*) $d/D = 0.08$; (*b*) $d/D = 0.10$ ($l = 30$ cm) for $D = 7$ cm. The red dashed lines stand for the theoretically calculated void fraction values.

$$E_{exp} = \sum_{1}^{i} n_i \varepsilon_{exp,i}, \tag{3.2}$$

where n is the number of rods, each one having a particular ε_{exp} value. In other words, the ε_{exp} values follow a linear additive rule although far from the correct ε_{th} values. This rule is further supported by subsequent measurements using multiple rods of small lengths (presented in figure 6). Furthermore, one may argue that if the number and dimensions of rods are not known in advance, it is difficult to determine accurately just from ERT tomographs the correct number and locations of the rods.

3.2. Rods of small lengths

The aim of these tests is to examine the ERT response when small-length objects are placed at different positions inside the test vessel. For this reason, rods of variable lengths (i.e. $l = 0.7$–6.0 cm) and of variable diameters (i.e. $d = 1.0$ and 2.3 cm) are used. To some extent, these smaller rods simulate the behaviour of actual multiphase systems with axially changing distributions (i.e. bubbly flows, oil-in-water flows, etc).

3.2.1. One rod: axial positioning. Figure 4(i) presents the effect of the rod diameter on the measured void fraction for rods having lengths comparable to the lengths of the electrodes ($l = 0.7$ cm). The rods are placed at several axial locations but always at the centre of the vessel cross-section ($r = 0$). Specifically, figure 4(i*a*) presents the ε_{exp} profiles for rods

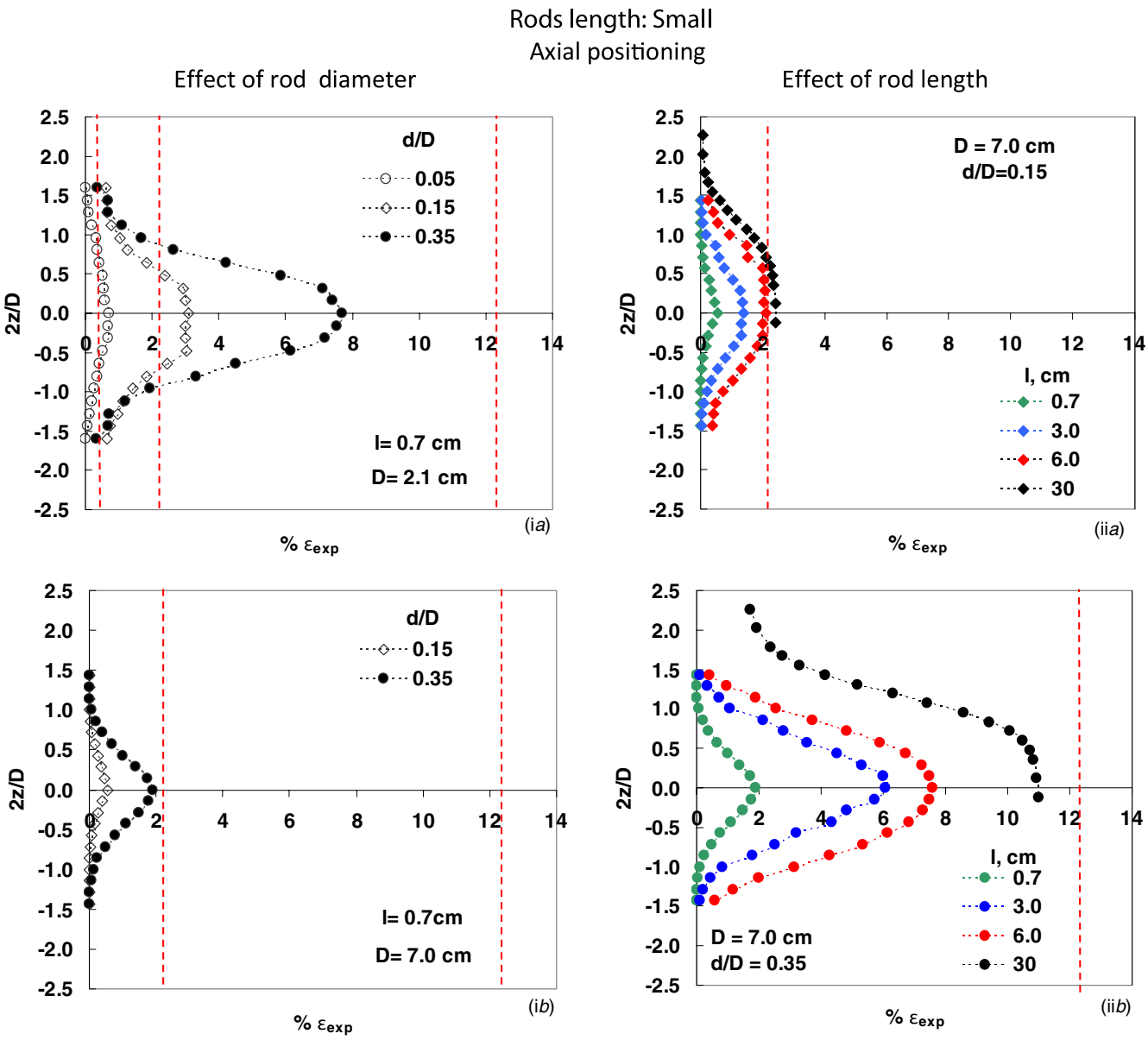

Figure 4. Void fractions during axial positioning of rods along the radial symmetry axis ($r = 0$); (i) same rod length ($l = 0.7$ cm) and variable rod *diameter* for different test vessels: (*a*) $D = 2.1$ cm, (*b*) $D = 7.0$ cm; (ii) same test vessel ($D = 7.0$ cm) and variable rod *length*: (*a*) $d/D = 0.15$, (*b*) $d/D = 0.35$. The red dashed lines stand for the theoretical void fraction value.

having the same length (i.e. $l = 0.7$ cm) but different diameters (i.e. $d/D = 0.05$, 0.15 and 0.35). Results are for the two test vessels having diameters $D = 2.1$ and 7.0 cm, figures 4(i*a*) and (i*b*), respectively. The dashed red lines represent the theoretical void fraction values, ε_{th}. Figure 4(i) shows that void fraction measurements follow a bell-shaped distribution around the plane defined by the geometrical centre of the electrodes ($z = 0$). The electrical field senses the presence of rods located far from the measurement plane (i.e. $2z/D > 0.5$) even for the smaller diameter rods. As the test vessel diameter decreases and the rod diameter increases, the electrical field spreads more above and below the electrode plane. This indicates that the expansion of the sensing field above and below the electrode plane (fringe effect) scales with the diameter of the vessel and the diameter of rods. It is noteworthy, however, that in both test vessels, the ERT signal tends to null at distances $2z/D$ higher than approximately ± 1.5 although the height of electrodes is not identical in the two vessels (0.5 cm for the $D = 2.1$ cm vessel and 0.7 cm for the $D = 7.0$ vessel). In any case, ε_{exp} values do not agree with ε_{th} values, even when the geometrical centre of the rods coincides with the geometrical centre of the electrodes ($2z/D = 0$). Interestingly, at this symmetry condition, in some cases ERT overestimates the void fraction, whereas in other cases it underestimates it. For instance, a combination of a small vessel diameter with a small rod diameter leads to overestimation of the void fraction.

Figure 4(ii) presents the effect of the rod length on void fraction measurement. Specifically, figure 4(ii) displays ε_{exp} profiles for rods displaced at several axial positions inside the test vessel ($D = 7.0$ cm) but always at the centre of the vessel cross-section ($r = 0$). The rods have various lengths (i.e. $l = 0.7$, 3.0 and 6.0 cm) and two different diameters

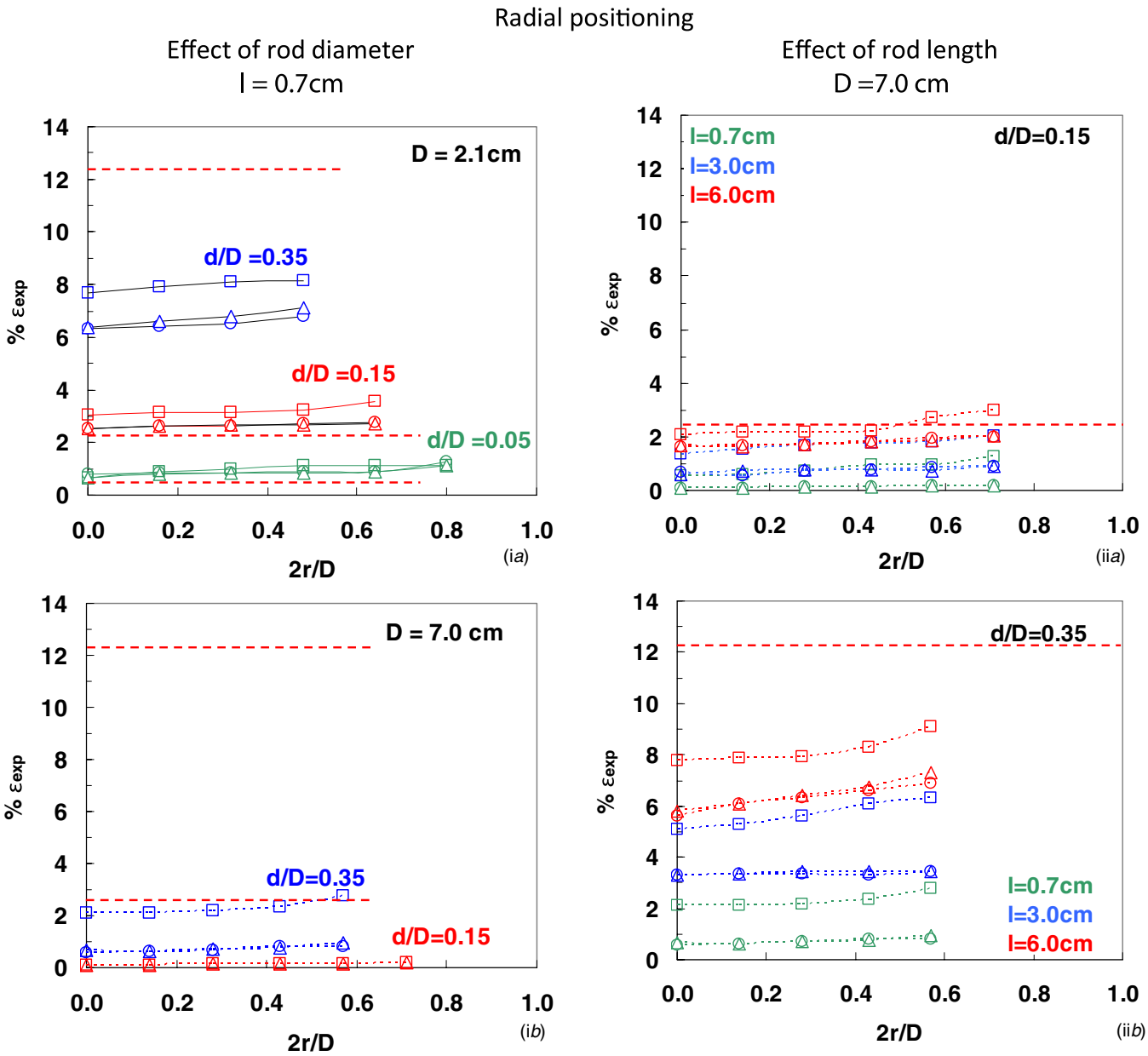

Figure 5. Void fractions during radial positioning of rods at different axial distances from the electrode plane ($z = 0$); (i) same rod length ($l = 0.7$ cm) and various rod *diameters*: (*a*) $D = 2.1$ cm, (*b*) $D = 7.0$ cm; (ii) same vessel diameter ($D = 7.0$ cm) and various rod *lengths*: (*a*) $d/D = 0.15$, (*b*) $d/D = 0.35$. The red dashed lines stand for the theoretical void fraction. The square, circle and triangle markers represent the three axial positions of the rods, i.e. $z = 2z/D = 0$, 0.5 and -0.5, respectively.

(i.e., $d/D = 0.15$ and 0.35). Results for each rod diameter are presented separately in figures 4(ii*a*) and (ii*b*). As in figure 4(i), void fraction measurements exhibit a bell-shaped distribution around the geometrical centre of the electrodes ($z = 0$).

As the length of the rod increases, ε_{exp} values increase approaching closer to ε_{th} values. For the smaller diameter rod (figure 4(ii*a*)), a rod of length 6 cm is long enough to bring ε_{exp} *close to* ε_{th} values. Much longer rods (30 cm) do not change this. In contrast, for the larger diameter rod (figure 4(ii*b*)), a 6 cm long rod does not suffice to yield correct ε_{exp} values. Correct values are found for a 30 cm long rod. Unfortunately, no intermediate rod diameters have been examined. To this end, it is evident that the fringe effect for the employed millimetre-size ERT electrodes is considerable and cannot be neglected if quantitative information is required from ERT data.

3.2.2. One rod: radial positioning. Figure 5 presents the effect of the radial displacement of rods of different diameters and lengths on void fraction measurement. Rods' radial displacement takes place at three different axial locations with respect to the electrode plane (i.e. $2z/D = 0$ and $2z/D = \pm 0.5$). The dashed red lines in all plots denote theoretical void fraction values, ε_{th}. Figures 5(i*a*) and (i*b*) display results for the small and the large test vessel cell (i.e. $D = 2.1$ and 7.0 cm), respectively. In all plots, it is clear that the measured void fraction increases slightly as the rods are radially displaced towards the wall of the vessel, that is, closer to the electrodes.

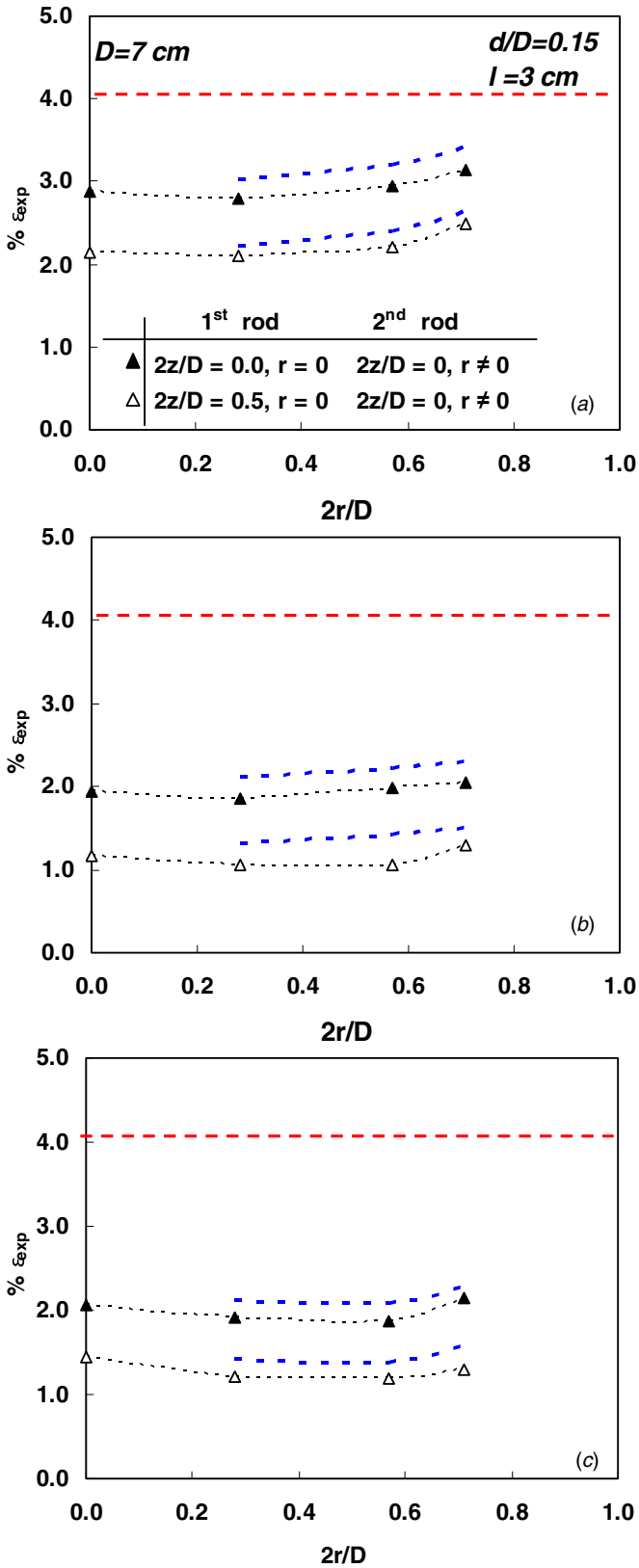

Figure 6. Void fraction distributions when two rods of equal diameter ($d/D = 0.15$) and length ($l = 3$ cm) are simultaneously placed inside the test vessel. The first rod is always at a fixed position at the centre of the pipe ($r = 0$), while the second rod is radially moving.

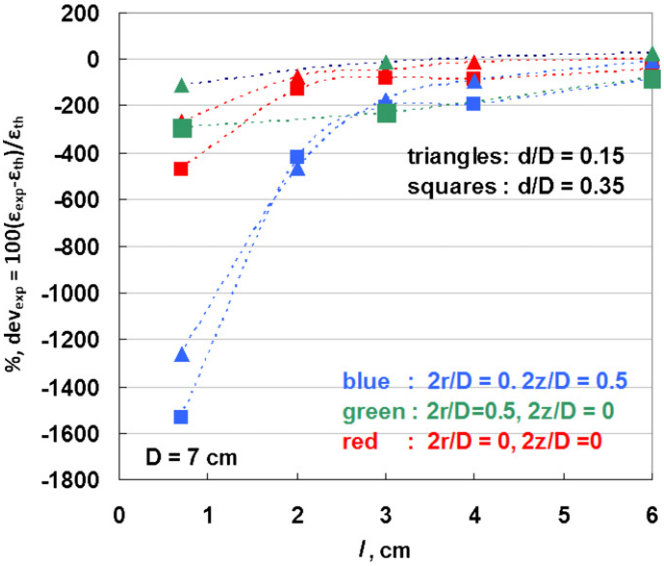

Figure 7. Influence of the rod lengths on the $\mathrm{dev}_{\mathrm{exp}}$ for two typical d/D values and for various radial and axial rod displacements.

The magnitude of this slight variation is alike for the examined three rod diameters and three axial locations (figure 5(i)) but increases a bit as the length of the rods increases (figure 5(ii)).

The $\varepsilon_{\mathrm{exp}}$ values for rods placed at $2z/D = +0.5$ at any radial position are similar to the ones obtained for rods placed at $2z/D = -0.5$ and the same radial position. This indicates that the axial symmetry of the sensing field described previously for $r = 0$ is valid for any other radial position inside the vessel. The smaller radial deviations in figure 5 than the axial deviations in figure 4 indicate that for the employed millimetre-size ERT electrodes, the distortion of the electric field due to the topography of the field strength at the cross-section of the electrode plane is less significant than the fringe effect.

3.2.3. Multiple rods. The objective of this section is to examine the ERT response in the case when two short rods are *simultaneously* placed inside the electrical field. Figure 6 presents the $\varepsilon_{\mathrm{exp}}$ values when *two* rods of the same diameter ($d/D = 0.15$) and length ($l = 3.0$ cm) are placed at different radial locations and axial locations with respect to the electrode plane (i.e. first rod's position: $r = 0$ and $z = 0, 0.5$, and second rod's position: several positions along the radial direction and $z = 0, 0.5$ and -0.5, figures 6(*a*), (*b*) and (*c*), correspondingly). The theoretical void fraction is again marked with a red dashed line. The dashed blue lines stand for the hypothetical void fraction value, calculated by adding the $\varepsilon_{\mathrm{exp}}$ values (already presented in figure 5(ii*a*)) that correspond to rods placed separately at the same positions as those presented in figure 6.

The observed radial variation is small in all combinations of the two rods. Contrary to figure 3, the $\varepsilon_{\mathrm{exp}}$ values in figure 6 are always much lower than the theoretical values. Moreover, $\mathrm{dev}_{\mathrm{exp}}$ increases as the rods are positioned away from the electrode plane ($2z/D = \pm 0.5$). It must be noted that even in the case when the first rod is placed at the electrode plane, where $\mathrm{dev}_{\mathrm{exp}}$ is minimum (figures 4 and 5), the presence of a second rod at a different axial position from $z = 0$ increases

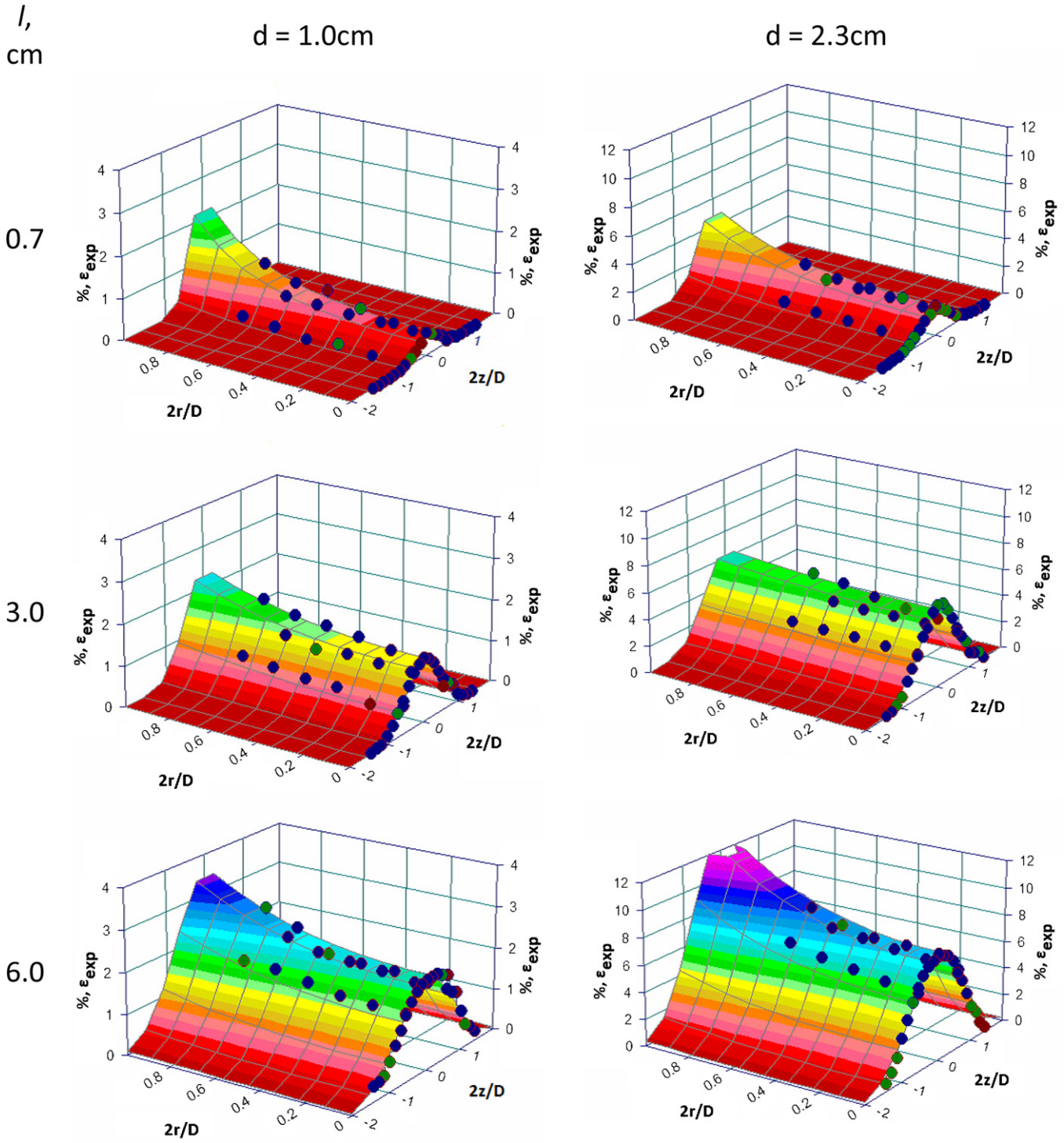

Figure 8. Best-fit surfaces of experimental void fractions with respect to the radial and axial coordinates for single rods of different diameters and lengths positioned inside the large test vessel ($D = 7.0$ cm).

dev_{exp}. Furthermore, the ε_{exp} values measured for the two rods are just a bit lower (dev $\sim 10\%$ for all examined cases) than the values derived when adding the ε_{exp} values corresponding to single rods (dashed blue lines). So, it seems that equation (3.2) is valid also for small-length rods.

We have seen so far that ε_{exp} values in most of the examined cases do not agree with ε_{th} values. In this paragraph, we collectively present this deviation for the large test vessel, $D = 7$ cm. Figure 7 displays the effect of the rod lengths on the dev_{exp} values, for two typical rod diameters (i.e. $d/D = 0.15$ and 0.35) and for various radial and axial distances of the (centre of the) rods from the (centre of the) electrode plane (i.e. $2r/D = 0$ and $2z/D = 0.5$; $2r/D = 0.5$ and $2z/D = 0$; $2r/D = 0$ and $2z/D = 0$). It is seen that the axial displacement of the rods away from the electrodes (blue markers) is the parameter that increases dev_{exp} dramatically (up to $\sim -1600\%$). This is really bad for the rod length of less than 2 cm. Radial displacement of the rods (green markers) has a smaller but still considerable

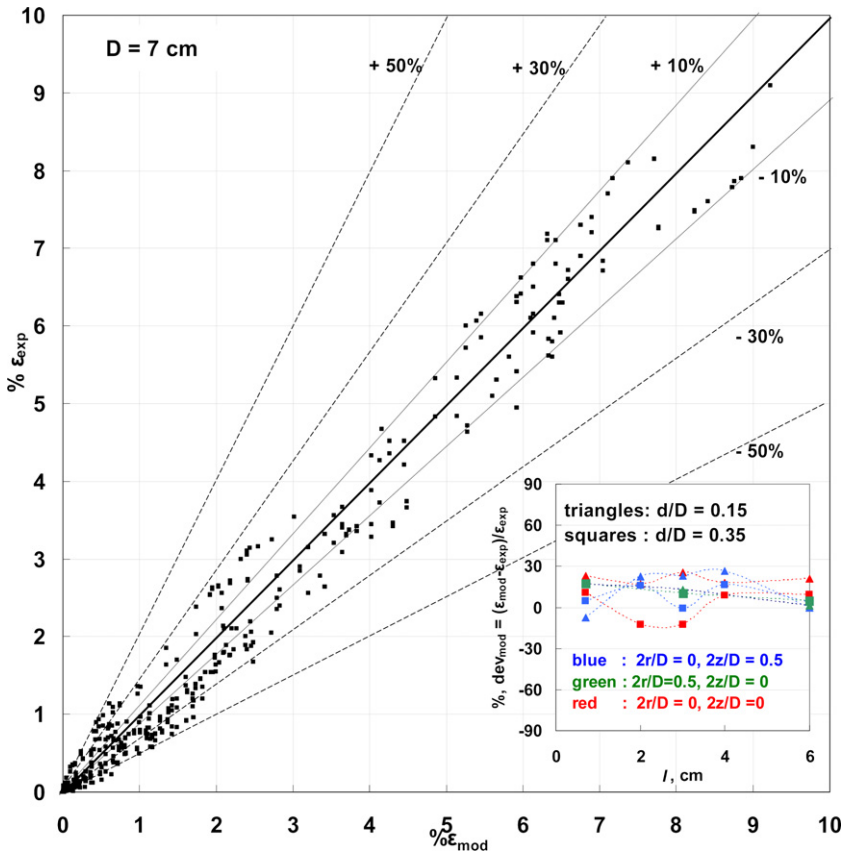

Figure 9. Parity plot between the experimental data and the model predictions (equations (3.3)–(3.8)). The small inset plot shows the % deviation between $\varepsilon_{\mathrm{mod}}$ and $\varepsilon_{\mathrm{exp}}$ values for two d/D ratios as a function of the rod lengths.

effect. Even with rods placed at the symmetry axes ($z = 0$; $r = 0$; red markers), there is still an appreciable $\mathrm{dev}_{\mathrm{exp}}$ especially for rods shorter than 2 cm. Overall, however, the symmetrical placement of rods leads to smaller deviations than those in non-symmetrical (axially/radially) placement. On the other hand, as the rod length increases, all deviations become smaller, and for rods 6 cm long, they do not exceed ~100%. The above are in line with figure 2, where 'infinitely' long rods placed at the symmetry plane ($z = 0$, $r = 0$) gave virtually zero $\mathrm{dev}_{\mathrm{exp}}$. Furthermore, this plot manifests that in the examined system the fringe effect (axial displacement) is far more important in distorting measurements than the topology of the field strength (radial displacement).

3.3. Model development

The aim of this section is to determine an empirical model capable of describing the experimental void fraction values, $\varepsilon_{\mathrm{mod}}$, for varying (a) electrode size, (b) test vessel diameter and (c) number/size/position of dispersed rods inside the ERT field. The proposed methodology can be applied to any soft-field measuring technique besides ERT. Nonlinear regression analysis of the measured void fractions versus the corresponding rod locations inside the ERT sensing field is conducted using TableCurve 3D v4.0® (SYSTAT®) for all the examined parameters. The software searches for the best fitted expression in a library of over 3000 nonlinear expressions. It is discovered that a squared exponential covariance (equation (3.3)) describes satisfactorily the experimental data (error less than $\pm 5\%$). The selection of this expression against others that give errors much smaller than $\pm 5\%$ is based on the small number of fitting parameters (a, b, c), which allows them a distinct physical context (see below), and on the observation that often $\pm 5\%$ is within the experimental scatter. Moreover, it is known (Barber 1989) that the distribution of electrical potential within a volume conductor through which a steady current flows is given by the solution of Poisson's equation, which reduces to Laplace's equation. The analytical solution of Laplace's equation can be reduced to exponential covariance functions (Borcea 2002):

$$\ln(\%\varepsilon_{\mathrm{mod}}) = a + b\left(\frac{2z}{D}\right)^2 + c\left(\frac{2r}{D}\right)^2. \tag{3.3}$$

Figure 8 shows the goodness of the fit for rods of two diameters and three lengths inside the large test vessel.

Next, a dimensionless analysis coupled with a multiple quasi-linear regression analysis is performed to correlate the a, b, c coefficients of equation (3.3) with the system's geometrical parameters, i.e. size and position of the rods, test vessel diameter and electrode dimensions (Bendat and Piersol 2000). The statistical significance of each coefficient was tested using the t-test with $P > 0.95$ (Draper and Smith 1981). It is found that the following set of equations fits the experimental data with an error less than $\pm$ 10%:

$$a = 6.6 + 0.64\ln(A_d) \tag{3.4}$$

$$b = -0.64 - \frac{0.016}{A_l^{0.5}} \tag{3.5}$$

$$c = -0.4 + 0.016[\ln A_l]^2. \tag{3.6}$$

A_d and A_l are the dimensionless numbers:

$$A_d = \frac{l_{\mathrm{el}} \cdot d_{\mathrm{el}}}{D^2} \frac{ld^2}{D^3} \tag{3.7}$$

$$A_l = \frac{l_{\mathrm{el}} \cdot d_{\mathrm{el}}}{D^2} \frac{l^2 d}{D^3}. \tag{3.8}$$

The predicted void fraction values, $\varepsilon_{\mathrm{mod}}$, estimated by the aforementioned set of equations are plotted against the experimental data in a parity plot (figure 9). It is seen that the proposed set of equations predicts the void fraction, with an overall accuracy better than $\pm$ ~10% for void fractions 2% $< \varepsilon_{\mathrm{mod}} <$10%. For 2% $< \varepsilon_{\mathrm{mod}} <$5%, the accuracy of the model is smaller ($\pm$ ~30%), and for $\varepsilon_{\mathrm{mod}} <$2%, the accuracy of the model is even smaller ($\pm$ ~50%). It is noteworthy that these deviations are much smaller than the deviations between $\varepsilon_{\mathrm{exp}}$ and $\varepsilon_{\mathrm{th}}$ (presented in figure 7). The small inset plot in figure 9 presents the deviations between $\varepsilon_{\mathrm{mod}}$ and $\varepsilon_{\mathrm{exp}}$ versus the rod lengths, having as parameters the rod diameters and the rod relative positions with respect to the electrode plane (see figure 7 for explanation). The term $\mathrm{dev}_{\mathrm{mod}}$ stands for the percentage deviation of the model values from the experimental ones and is estimated using equation (3.9):

$$\mathrm{dev}_{\mathrm{mod}} = 100 \times \frac{\varepsilon_{\mathrm{mod}} - \varepsilon_{\mathrm{exp}}}{\varepsilon_{\mathrm{exp}}}. \tag{3.9}$$

Evidently, deviations are independent of the value of the rod length as well as the values of the other parameters. This supports the validity of the model over a broad range of conditions.

Equation (2.1) and the set of equations (3.3)–(3.9) can be used to search for the optimum electrode sizes that yield $\varepsilon_{\mathrm{mod}}$ values equal to $\varepsilon_{\mathrm{th}}$ values ($\mathrm{dev}_{\mathrm{mod}} = 0$). In this case,

$$\varepsilon_{\mathrm{th}} = \frac{A_{\mathrm{obj}}}{A_{\mathrm{test}}} = \left(\frac{d}{D}\right)^2 = \varepsilon_{\mathrm{mod}}. \tag{3.10}$$

The simplest case is when the rods are placed symmetrically as regards the electrode plane ($2z/D = 2r/D = 0$). At this particular rod placement, both the fringe effect and the topology of the field's strength diminish (figure 7). For this case, solving equation (3.10) leads to the following expression:

$$(l_{\mathrm{el}} d_{\mathrm{el}})_{\mathrm{opt}} = 0.0443 \times \frac{d^{\frac{9}{8}} D^{\frac{15}{8}}}{l}. \tag{3.11}$$

Equation (3.11) allows a parametric analysis of ERT measurements. Specifically, equation (3.11) suggests that there is an optimum surface area of the electrodes, $(l_{\mathrm{el}}\, d_{\mathrm{el}})_{\mathrm{opt}}$, that yields measurements 'close to' the theoretically expected void fraction values. The phrase 'close to' refers to (a) the error associated with the experiments (measurement noise, variability of repetitions) and (b) the goodness of the fit through the data (figure 7). Figure 10 presents the dependence of $(l_{\mathrm{el}}\, d_{\mathrm{el}})_{\mathrm{opt}}$ on the rod dimensions (length and diameter) and on the test vessel diameter. The red dashed lines stand for the particular $l_{\mathrm{el}}\, d_{\mathrm{el}}$ values employed in this study. For

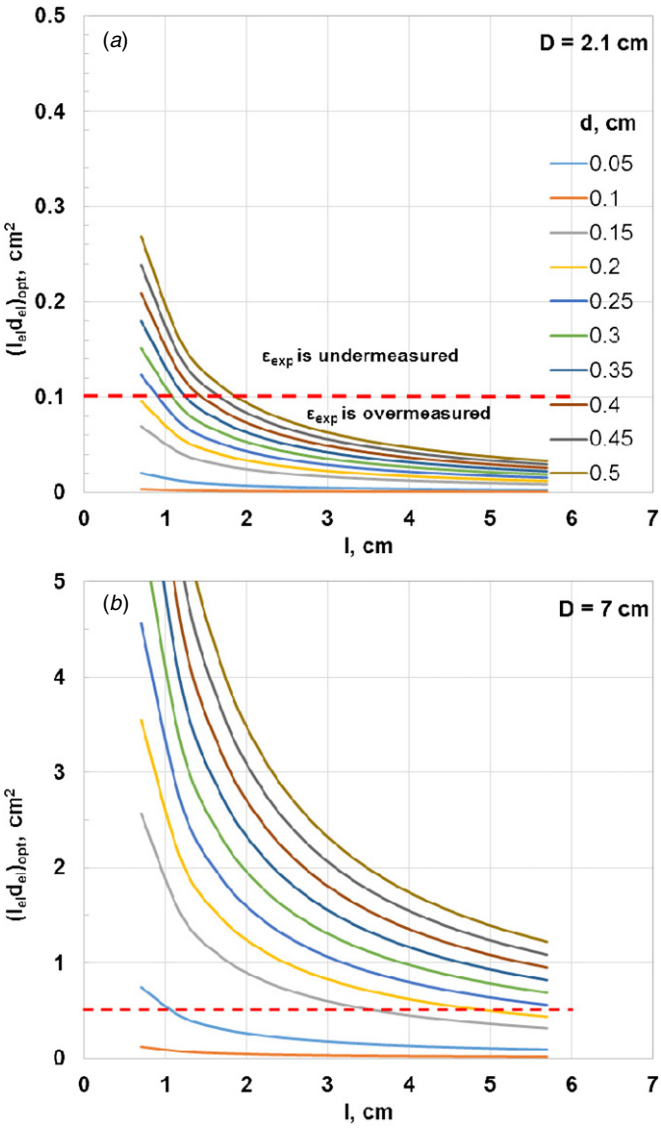

Figure 10. Optimum surface area of electrodes, $(l_{\mathrm{el}} d_{\mathrm{el}})_{\mathrm{opt}}$, for yielding $\varepsilon_{\mathrm{th}}$, displayed with respect to the rod lengths and for various rod diameters. Results are presented separately for each test vessel diameter: (*a*) 2.1 and (*b*) 7 cm. The dashed red lines represent the $l_{\mathrm{el}} d_{\mathrm{el}}$ values employed in this study.

any combination of (l, d, D), there is always a unique $(l_{\mathrm{el}}\, d_{\mathrm{el}})_{\mathrm{opt}}$ that leads to the correct void fraction values ($\varepsilon_{\mathrm{th}}$). If the employed $l_{\mathrm{el}}\, d_{\mathrm{el}}$ value is larger than $(l_{\mathrm{el}}\, d_{\mathrm{el}})_{\mathrm{opt}}$, then $\varepsilon_{\mathrm{exp}}$ will be smaller than $\varepsilon_{\mathrm{th}}$ (overmeasured). Vice versa, if $l_{\mathrm{el}}\, d_{\mathrm{el}}$ is smaller than $(l_{\mathrm{el}}\, d_{\mathrm{el}})_{\mathrm{opt}}$, then $\varepsilon_{\mathrm{th}}$ is undermeasured. Moreover, $(l_{\mathrm{el}}\, d_{\mathrm{el}})_{\mathrm{opt}}$ values increase as the rod length decreases or the rod diameter increases. Furthermore, $(l_{\mathrm{el}}\, d_{\mathrm{el}})_{\mathrm{opt}}$ becomes more sensitive to the diameter of the rods as the length of the rods gets smaller. For the small test vessel ($D = 2.1$ cm, figure 10(*a*)) and for $l >$ ~4 cm, $(l_{\mathrm{el}}\, d_{\mathrm{el}})_{\mathrm{opt}}$ takes too small values, which poses technical difficulties in constructing the electrodes and placing them flush with the vessel wall.

Figure 10 explains observations made earlier (e.g. figures 3, 4 and 6) where $\varepsilon_{\mathrm{exp}}$ values were occasionally overmeasured or undermeasured. Equation (3.11) might be useful for improving the performance of the ERT technique

as it suggests the proper size of electrodes according to every application's particular needs (e.g. measurement of objects within a specific size range in a specific pipe diameter).

4. Conclusion

This study provides experimental evidence of the influence of certain geometrical parameters on the accuracy of ERT measurements in two-phase systems. It is seen that for homogeneously (axially and radially) dispersed rods the void fraction measured by a set of electrodes at a plane agrees pretty well with 2D theoretical predictions ($\mathrm{dev}_{\mathrm{exp}} < \pm 10\%$). However, in cases of non-homogeneously dispersed rods, void fraction measurements deviate *considerably* from theoretical values (max. $\mathrm{dev}_{\mathrm{exp}} \sim 1600\%$). Responsible for this deviation are the fringe effect and the topography of the ERT field strength at the cross-section of the electrode plane. These two effects are assessed separately by varying the placement of rods in the axial and radial directions with respect to the electrode plane. It is found that for the employed millimetre-size ERT electrodes, the fringe effect is considerable and cannot be neglected if quantitative information is required from ERT data. Nevertheless, the effect of the topography of the field strength is less significant than the fringe effect.

Nonlinear regression of the present data yields an empirical model that describes the void fraction measured by ERT (max. $\mathrm{dev}_{\mathrm{mod}} < \pm 50\%$) at different axial and radial positions of the Teflon rods inside the test vessel and for all examined parameters (i.e. diameter of test vessel, size of electrodes, number and size (radius and length) of submerged Teflon rods). Moreover, dimensional analysis coupled with multiple quasi-linear regressions allows us to correlate the parameters of the model with real geometrical characteristics of the system giving them a distinct physical context. A parametric study of this model permits appraisal of the different geometrical characteristics on measurements and even suggests an optimum surface area of electrodes in order to measure values close to theoretical 2D predictions. The proposed methodology can be used to improve the accuracy of future ERT systems but can also be applied to any soft-field measuring technique besides ERT.

Acknowledgment

This study was carried out under the umbrella of COST Action MP1106: 'Smart and green interfaces—from single bubbles and drops to industrial, environmental and biomedical applications'.

References

Alaqqad M, Bennington C P J and Martinez D M 2012 An estimate of the axial dispersion during flow through a compressible wood-chip bed *Can. J. Chem. Eng.* **90** 1602–11

Barber D C 1989 A review of image reconstruction techniques for electrical impedance tomography *Med. Phys.* **16** 162–9

Bendat J S and Piersol A G 2000 *Random Data Analysis and Measurement Procedures* 3rd edn (New York: Wiley)

Borcea L 2002 Electrical impedance tomography *Inverse Problems* **18** R99–136

Chin R K Y 2011 Tomographic imaging using *ad hoc* and mobile sensors *PhD Dissertation* University of Manchester

Dobecki T L and Upchurch S B 2006 Geophysical applications to detect sinkholes and ground subsidence *Leading Edge* **25** 336–41

Draper N R and Smith H 1981 *Applied Regression Analysis* 2nd edn (New York: Wiley)

Fan W R and Wang H X 2010 Maximum entropy regularization method for electrical impedance tomography combined with a normalized sensitivity map *Flow Meas. Instrum.* **21** 277–83

Fransolet E, Crine M, L'Homme G, Toye D and Marchot P 2002 Electrical resistance tomography sensor simulations: comparison with experiments *Meas. Sci. Technol.* **13** 1239–47

George D L, Torczynski J R, Shollenberger K A and O'Hern T J 2000 Validation of electrical-impedance tomography for measurements of material distribution in two-phase flows *Int. J. Multiph. Flow* **26** 549–81

Karapantsios T D and Papara M 2008 On the design of electrical conductance probes for foam drainage applications. Assessment of ring electrodes performance and bubble size effects on measurements *Colloids Surf.* A **323** 139–48

Kim B S, Khambampati A K, Hong Y J, Kim S and Kim K Y 2013 Multiphase flow imaging using an adaptive multi-threshold technique in electrical resistance tomography *Flow Meas. Instrum.* **31** 25–34

Kim B S, Khambampati A K, Kim S and Kim K Y 2011 Image reconstruction with an adaptive threshold technique in electrical resistance tomography *Meas. Sci. Technol.* **22** 104009

Kim B S, Khambampati A K, Kim S and Kim K Y 2012 Improving spatial resolution of ERT images using adaptive mesh grouping technique *Flow Meas. Instrum.* **31** 19–24

Kostoglou M, Varka E-M, Kalogianni E P and Karapantsios T D 2010 Evolution of volume fractions and droplet sizes by analysis of electrical conductance curves during destabilization of oil-in-water emulsions *J. Colloid Interface Sci.* **349** 408–16

Li Y and Yang W 2009 Measurement of multi-phase distribution using an integrated dual-modality sensor *IST'09: Proc. IEEE Int. Workshop on Imaging Systems and Techniques* p 335

Pikkemaat R, Tenbrock K, Lehmann S and Leonhardt S 2012 Electrical impedance tomography: new diagnostic possibilities using regional time constant maps *Appl. Cardiopulm. Pathophysiol.* **16** 212–25

Polydorides N 2002 Image reconstruction algorithms for soft-field tomography *PhD Dissertation* University of Manchester

Sharifi M and Young B 2013 Electrical resistance tomography (ERT) applications to chemical engineering *Chem. Eng. Res. Des.* **91** 1625–45

Stanley S J, Mann R and Primrose K 2002 Tomographic imaging of fluid mixing in three dimensions for single-feed semi-batch operation of a stirred vessel *Chem. Eng. Res. Des.* **80** 903–9

Sun J and Yang W 2012 3D effect of electrical capacitance and resistance tomography sensors *IST'12: Proc. IEEE Int. Conf. on Imaging Systems and Techniques* p 562

Sun J and Yang W 2013 Fringe effect of electrical capacitance and resistance tomography sensors *Meas. Sci. Technol.* **24** 074002

Wang Q, Wang H, Cui Z and Yang C 2012 Reconstruction of electrical impedance tomography (EIT) images based on the expectation maximum (EM) method *ISA Trans.* **51** 808–20